

# High Fidelity Interactive Video Segmentation Using Tensor Decomposition, Boundary Loss, Convolutional Tessellations, and Context-Aware Skip Connections

Anthony D. Rhodes  
Intel Corporation  
anthony.rhodes@intel.com

Manan Goel  
Intel Corporation  
manan.goel@intel.com



Figure 1: Rendered segmentation (left); input image, 2k resolution (right).

## ABSTRACT

We provide a high fidelity deep learning algorithm (HyperSeg) for interactive video segmentation tasks using a convolutional network with *context-aware skip connections*, and compressed, "hypercolumn" image features combined with a *convolutional tessellation* procedure. In order to maintain high output fidelity, our model crucially processes and renders all image features in high resolution, without utilizing downsampling or pooling procedures. We maintain this consistent, high grade fidelity efficiently in our model chiefly through two means: (1) We use a statistically-principled, tensor decomposition procedure to modulate the number of hypercolumn features and (2) We render these features in their native resolution using a convolutional tessellation technique. For improved pixel-level segmentation results, we introduce a boundary loss function; for improved temporal coherence in video data, we include temporal image information in our model. Through experiments, we demonstrate the improved accuracy of our model against baseline models for interactive segmentation tasks using high resolution video data. We also introduce a benchmark video segmentation dataset, the *VFX Segmentation Dataset*, which contains over 27,046 high resolution video frames, including green screen and various composited scenes with corresponding, hand-crafted, pixel-level segmentations. Our work presents an extension to improvement to state of the art segmentation fidelity with high resolution data and can be used across a broad range of application domains, including VFX pipelines and medical imaging disciplines.

## CCS CONCEPTS

• Computing methodologies → Video segmentation.

## KEYWORDS

Computer Vision, Object Segmentation, Interactive Segmentation, Model Compression

## ACM Reference Format:

Anthony D. Rhodes and Manan Goel. 2020. High Fidelity Interactive Video Segmentation Using Tensor Decomposition, Boundary Loss, Convolutional Tessellations, and Context-Aware Skip Connections. In *Proceedings of the 16th ACM SIGGRAPH European Conference Visual Media Production (CVMP 2020)*. ACM, New York, NY, USA, 8 pages. <https://doi.org/10.1145/1122445.1122456>

## 1 INTRODUCTION

Image segmentation has a long history in computer vision and remains today an essential and largely unsolved problem. Prior to the advent of deep learning, classical methods for image segmentation included techniques such as thresholding [27],[44], clustering [12],[11] compression [50], [2], histogram-based approaches [34], watershed [33], region-growing [1], in addition to techniques utilizing hand-crafted features, including [31], [13], [20] – to name a small number of methods. More recently, many algorithms employing energy minimization frameworks, including graph cuts [6], Markov Random Fields [14], and related probabilistic graphic models [14] have been implemented successfully.

With the adoption of deep learning, convolutional neural networks (CNNs) [26], [25] have become a standard model for data-driven approaches to computer vision tasks. Due to the early primacy of deep classification models across computer vision, many deep learning segmentation and localization algorithms rely on the appropriation of pre-trained classifiers as a key ingredient in their workflows. In particular, so-called region-proposal and related regression-classification methods [52], including R-CNN [17], Fast R-CNN [16], Faster R-CNN [38], FPN [30], and Yolo [37], all generate approximate, coarse-level object detections (i.e. bounding-boxes) for a set of class-specific objects. More recently still, deep learning classification pipelines have inspired methods in semantic segmentation tasks (i.e. pixel-level segmentation for class-specific objects) using "fully convolutional" networks; these approaches include, notably, FCN [40], Mask-RCNN [22], U-Net [39], and Deeplab (v2, v3) [8].

In recent years, interactive video and interactive image segmentation have emerged as key components of advanced image editing, graphics effects and medical imaging applications [46], [28], [45]. Segmentation problems, including rotoscoping for vfx workflows [47] and bio-medical image annotation [54] represent essential, labor-intensive image-processing tasks today which rely crucially on human-computer interaction.

Fully automated methods for interactive segmentation present a significant challenge because of the inherent ambiguity, multi-modality and complexity underlying pixel-level segmentation tasks, making these approaches largely infeasible. On the other hand, interaction-intensive methods conversely run the risk of requiring too much time, making them impractical in general. For these reasons, most researchers follow a semi-supervised approach to segmentation problems. In this setting, user interaction is commonly instantiated in the form of a set of user clicks, typically consisting of both *positive* clicks (i.e. clicks within the object of interest/foreground) and *negative* clicks (i.e. clicks indicating background pixels); alternatively, strokes, splines or partial segmentations are also often used as modalities of user interaction [43], [6], [49]. Video segmentation is often more difficult than image segmentation due to the occurrence of motion blur, occlusion, and the temporal coherence requirements of consecutive segmentations [4].

In contrast to semantic segmentation tasks for class-specific objects, interactive segmentation represents a class-agnostic, few-shot active learning paradigm [29]. Seen in this way, the segmentation model is tasked with determining the appropriate pixel classification (i.e. foreground/background) based on a relatively small number of labeled examples provided by the user. Fully-convolutional networks (FCN), trained end-to-end on input images and segmentation masks, have been shown to successfully synthesize low-level features (e.g. textures, color information) with high-level features such as objectness and semantic information robustly for few-shot vision tasks, including interactive segmentation [40], [29]. Several approaches rely on improving this synthesis by applying a post-processing technique following an initial DNN approximate segmentation [8]; [9] combine FCNs with a CRF for boundary refinement, while [53] combine FCNs with RNNs as approximate mean-field inference.

Our work presents a single, high capacity FCN for end-to-end

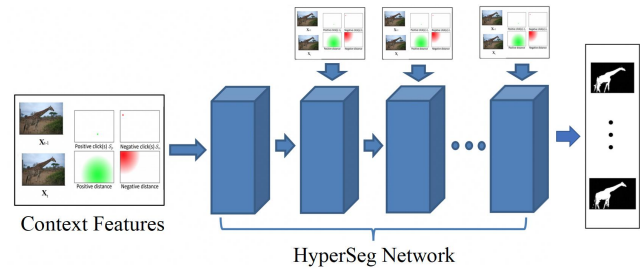


**Figure 2: Segmentation network with context-aware skip connections schematic.**

interactive video segmentation, building significantly on [29]. This research draws upon several related works, including in particular: DOS (Deep Interactive Object Segmentation) [48] which learns high-level objectness using a FCN with features generated by applying a distance transform to user clicks; [40] who employ a skip architecture in conjunction with an FCN to propagate semantic information for segmentation; and [29], which is most closely related to our work, and incorporates latent diversity into a single FCN to improve output segmentation quality.

In total, our research provides the following contributions: (1) We apply tensor decomposition to a set of dense convolutional features to achieve substantial model compression, while maintaining segmentation fidelity; (2) We define a novel boundary loss function to improve segmentation quality along the periphery of an object; (3) We introduce a convolutional tessellation technique to render pre-trained features in the native input resolution; (4) We design our network to incorporate "context-aware" skip connections, which propagate the input image and interactive features across the model, thereby avoiding the dilution of these features in the latter layers of the network; (5) Lastly, we present a new benchmark video segmentation dataset, the *VFX Segmentation Dataset*, containing 27,046 high resolution video frames with pixel-level ground-truth segmentations for training and testing segmentation models.

In the following sections, we present the details of our algorithm, followed by a comparative evaluation with several baseline and state of the art models on high resolution data. Our experiments demonstrate that the present approach outperforms the comparative models with respect to both overall segmentation accuracy (IOU – intersection over union) and boundary segmentation accuracy (BIOU). In addition, in contrast to the comparison models, our model is the only network that processes the input data in its native resolution.

## 2 OVERVIEW

Our objective is to design a network  $f$  that receives as input consecutive color images  $\mathbf{X}_{t-1}, \mathbf{X}_t \in \mathbb{R}^{w \times h \times 3}$  from video data in addition to user click features, and produces a binary mask that appropriately segments the object of interest indicated by the user. Concretely, if we denote the input representation of the network as  $\mathbf{X}'$ , our goal is to train  $f$  so that  $f(\mathbf{X}') = \mathbf{Y} \in [0, 1]^{w \times h}$ , where the final binary output segmentation is generated by thresholding  $\mathbf{Y}$  at  $1/2$ .

Layer	Convolution	Dilation	Pad	Input	Depth
1	1 × 1	1	0	746	70
2	3 × 3	1	0	80	70
3	3 × 3	2	2	80	70
4	3 × 3	4	4	80	70
5	3 × 3	8	8	80	70
6	3 × 3	16	16	80	70
7	3 × 3	32	32	80	70
8	3 × 3	64	64	80	70
9	3 × 3	128	128	80	70
10	3 × 3	1	0	80	6

## 2.1 Segmentation Network

**2.1.1 Network Architecture.** The input to our network  $f$  includes the current and previous input frames,  $X_t$  and  $X_{t-1}$ , and binary positive and negative user click masks  $B_p, B_n \subset \{0, 1\}^{w \times h}$ . In addition, as in [29], we include diffusion maps  $D_p$  and  $D_n$  based on a distance transform applied to the binary user click masks; to this end, we define:  $D_n(\mathbf{p}) = \min_{\mathbf{q} \in S_n} \|\mathbf{p} - \mathbf{q}\|_2$  and  $D_p(\mathbf{p}) = \min_{\mathbf{q} \in S_p} \|\mathbf{p} - \mathbf{q}\|_2$ .

We furthermore apply a VGG-19 network [41] pretrained on the ImageNet dataset [15] to the image  $X_t$  as part of a convolutional tessellation procedure, which we denote  $T(\cdot)$  and detail in Section B. These feature maps are then upsampled to the resolution of  $X_t$  using a *nearest-neighbor* approximation. After generating these pre-trained features for the input image, we subsequently apply a tensor decomposition to these dense feature maps, denoted by the mapping  $\phi(\cdot)$ , and described in Section C. In total, the final input to our network consists of the previous and current input frames  $X_{t-1}, X_t$ , binary user click masks  $B_p, B_n$ , diffusion maps  $D_p, D_n$ , and pre-trained features of the input image following the the convolution tessellation procedure and tensor decomposition algorithm, indicated by  $T(\phi(X_t))$ . The input to the network consist of 746 total features at resolution  $1920 \times 1080$  (736 pre-trained features and 10 "context" features, including  $X_{t-1}, X_t, B_p, B_n, D_p$  and  $D_n$ ). Each subsequent layer in the network has output depth 70 and input dimension 80 (70 features from the previous layer output + 10 features comprising the context-aware skip connections).

The core architecture of the HyperSeg network is a context aggregation network (CAN) [10], [51]. In the first layer of the network, we apply an affine projection at full resolution (using  $1 \times 1$  convolutions), where each per-pixel hypercolumn input feature is mapped to  $\mathbb{R}^{70}$ . In the subsequent layers of the network we apply  $3 \times 3$  convolutions with increasingly larger dilations at full resolution, followed by RELU activation [32]. In addition, each layer after the first layer receives the aforementioned input "context" features via skip connections (see Table 1 and Section D). As in [29], our network generates a diverse set of  $M$  potential segmentations, where the network is trained to exploit the inherent multimodality of plausible object segmentations extant in the model latent space. As [29] show, exploiting this latent diversity results in significant improvements in pixel-level segmentation accuracy.

**2.1.2 Loss Function.** We train the network  $f$  on a loss function [29] augmented with a novel component we term "boundary loss";

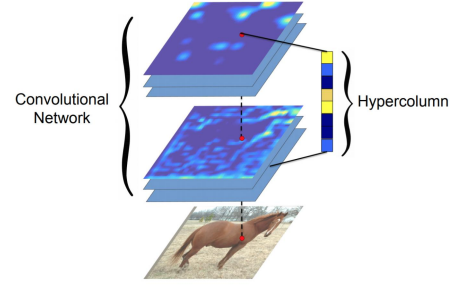


**Figure 3: Example of dense, hyper-column image features generated by CNN. Image credit [21]**

we define boundary loss:

$$\sum_i \sum_{m=1}^M l_{\partial\text{-PHL}}(Y_i, f_m(X_i; \theta_f)) \quad (1)$$

where the outer sum is over the dataset, and the inner sum is over the  $M$  segmentations produced by the network;  $Y_i$  denotes the ground truth segmentation of the  $i$ th datum, and  $f_m(X_i; \theta_f)$  indicates the  $m$ th segmentation produced by the network with respect to the  $i$ th datum. We use the subscript  $l_{\partial\text{-PHL}}$  to stipulate use of the *pseudo-Huber loss* [3] applied to the *boundary* (where  $\partial$  denotes the boundary operator, i.e., we extract the largest peripheral contour of the given segmentation). The purpose of this additional loss function is to strongly encourage boundary points in the generated segmentation to match the ground-truth.

We define the *boundary pseudo-Huber loss function* as follows:

$$l_{\partial\text{-PHL}}(Y, f_m(X_i; \theta_f)) = \sum_{\mathbf{p} \in \partial(f_m(X_i; \theta_f))} \delta^2 \left( \sqrt{1 + ((Y(\mathbf{p}) - f_m(X_i; \theta_f)_{\mathbf{p}}) / \delta)^2} - 1 \right) \quad (2)$$

where the sum is performed over  $\mathbf{p} \in \partial(f_m(X_i; \theta_f))$ , indicating the set of points along the boundary of the  $m$ th segmentation generated by our network for the  $i$ th datum. We use the notation  $f_m(X_i; \theta_f)_{\mathbf{p}}$  to indicate the value of the generated segmentation at the boundary point  $\mathbf{p}$ . Pseudo-Huber loss combines the strengths of both  $L_1$  and  $L_2$  losses; the parameter  $\delta$  controls the steepness of the loss function. In our experiments we use a relatively large  $\delta$  value in order to severely penalize boundary segmentation errors.

Using this definition of boundary loss, we define the following total loss function for our segmentation network:

$$\mathcal{L}_f(\theta_f) = \sum_i \min_m \left\{ l(Y_i, f_m(X_i; \theta_f)) + l_{IC}(S_p^i, S_n^i, f_m(X_i; \theta_f)) \right\} + \sum_i \sum_{m=1}^M \lambda_{ml} l(Y_i, f_m(X_i; \theta_f)) + \sum_i \sum_{m=1}^M l_{\partial\text{-PHL}}(Y_i, f_m(X_i; \theta_f)) \quad (3)$$

where above the first three terms of the loss function denote *Jaccard loss*, *interactive-context loss* and *ranked diversity loss*, respectively, as defined in [29].

Jaccard loss [5] is a relaxation of IOU, defined for segmentation masks  $A$  and  $B$ :

$$l(A, B) = 1 - \frac{\sum_{\mathbf{p}} \min(A(\mathbf{p}), B(\mathbf{p}))}{\sum_{\mathbf{p}} \max(A(\mathbf{p}), B(\mathbf{p}))} \quad (4)$$

In order to enforce agreement between the segmentation generated by our network and the user interaction provided via positive and negative clicks, we use an interactive-context loss function:

$$l_{IC}(S_p^i, S_n^i, A) = \|S_p \odot (S_p - A)\|_1 + \|S_n \odot (S_n - (1 - A))\|_1 \quad (5)$$

here  $\odot$  represents elementwise product.

Lastly, [29] demonstrate the utility of incorporating a ranked diversity loss function which imposes an ordering on the  $M$  segmentations rendered by the network. This ordering is effectuated by multiplying each Jaccard loss term,  $l(Y_i, f_m(\mathbf{X}_i; \theta_f))$ , by a scalar value  $\lambda_m$  from a decreasing sequence, which we define:  $\lambda_m = 10^{-2} \cdot 2^{M-m}$  for  $1 \leq m \leq M$ . The effect of this ranked diversity loss function is to compel the model to break symmetries between solutions and to thereby consistently order the segmentations according to their accuracy (i.e. segmentation  $m = 1$  will in general produce the most accurate segmentation of the  $M$  total segmentations produced by our network).

## 2.2 Dense Feature Compression

Prior to passing the input image  $\mathbf{X}_t$  through our segmentation network, we first generate image features from a pre-trained VGG-19 network. To do so, we pass  $\mathbf{X}_t$  through the pre-trained network and extract feature maps from the following layers: ‘conv1\_2’, ‘conv2\_2’, ‘conv3\_2’, ‘conv4\_2’, and ‘conv5\_2’ (denoted  $C_1, C_2, C_3, C_4, C_5$ , respectively). Next we upsample these features to the resolution of  $\mathbf{X}_t$  using a *nearest-neighbor* approximation, yielding a dense stack of hypercolumn features  $H_f$  of dimension  $1920 \times 1080 \times 1477$  [21]. We show a depiction of dense, hypercolumn features in Figure 3. Our network uses these dense, per-pixel VGG-19 features to account for the high degree of complexity inherent to pixel-level segmentation tasks. The downside, naturally, of using these dense features is their considerable memory cost.

To reduce the memory and parameter overhead of our network, we apply a tensor decomposition to each of the tensors  $C_1, C_2, C_3, C_4, C_5$ . Concretely, we utilize a *Higher Order Singular Value Decomposition* (HOSVD) [21],[19] algorithm known as *Tucker decomposition* [24], [36] to specifically reduce the filter depth of each of these convolutional tensors. The goal of this compression is to diminish the overall depth of  $H_f$  in a statistically-principled way whilst preserving the richness of the reduced VGG features inputted into our segmentation network; we refer to this compressed dimension as  $D_\phi$ . In our experiments we apply a roughly  $2X$  compression rate using Tucker decomposition, yielding a compressed version of  $H_f$  with dimension  $1920 \times 1080 \times 736$  (i.e.  $D_\phi = 736$ ).

In general, for an  $N$ -tensor, Tucker decomposition is framed as the problem of finding the decomposition of a tensor  $\mathbf{X} \in \mathbb{R}^{R_1 \times \dots \times R_N}$ , with  $\mathbf{G} \in \mathbb{R}^{R'_1 \times \dots \times R'_N}$ , and  $\mathbf{A}^{(1)} \in \mathbb{R}^{R_1 \times R'_1}$ , ...,  $\mathbf{A}^{(N)} \in \mathbb{R}^{R_N \times R'_N}$ , where  $1 \leq R'_i \leq R_i$  for  $1 \leq i \leq N$ , with the optimization constraint:

$$\min_{\hat{\mathbf{X}}} \|\mathbf{X} - \hat{\mathbf{X}}\| \text{ with } \hat{\mathbf{X}} = \sum_{r_1=1}^{R_1} \dots \sum_{r_N=1}^{R_N} g_{r_1 \dots r_N} \mathbf{a}_{r_1}^{(1)} \otimes \dots \otimes \mathbf{a}_{r_N}^{(N)} \quad (6)$$

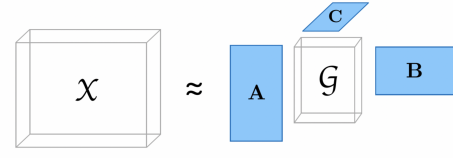


**Figure 4: Depiction of 3-Tensor Tucker decomposition. Here  $\mathbf{G}$  is the core tensor and  $\mathbf{A}$ ,  $\mathbf{B}$ , and  $\mathbf{C}$  are the principal components of the decomposition of tensor  $\mathbf{X}$ . Image credit [36].**

where  $\otimes$  connotes the tensor product;  $\mathbf{G}$  is known as the *core tensor* and the factor tensors  $\mathbf{A}^{(1)}, \dots, \mathbf{A}^{(N)}$  are called the *principal components* of the decomposition. Compression is achieved when  $R'_i < R_i$  for at least one axis of the tensor (note the strict inequality). In particular, because we wish to reduce the filter depth in each convolutional layer that we extract from VGG-19 while maintaining the original input image resolution, we apply the decomposition to each convolutional tensor along solely the depth axis. Figure 3 depicts a 3-tensor Tucker decomposition.

## 2.3 Convolutional Tessellations

Most standardized pre-trained deep models used in computer vision for feature extraction are classifiers (e.g., VGG [41], Resnet [23], Inception [42], etc.) trained on relatively low-resolution image data (ImageNet, for instance, has an average resolution of  $462 \times 387$ ). The input resolutions of these standardized deep models are accordingly generally quite low – for example, VGG-19 and Resnet both have input resolution  $224 \times 224$ ). This low input image resolution can significantly impact the fidelity of the resultant features rendered by the deep network (see Figure 5).

Pixel-level segmentation in high-resolution domains requires a very fine-grain output. As such, low-fidelity pre-trained features present a substantial barrier to improving deep learning models across a broad range of computer vision applications. We provide a simple and elegant solution to this problem using a convolutional tessellation algorithm.

Given an input image  $\mathbf{X}_t$  of dimension  $w \times h$  and pre-trained model  $M$  (e.g. VGG) with input resolution  $w_M \times h_M$  we first interpolate  $\mathbf{X}_t$  to dimension:  $w_m \lceil \frac{w}{w_M} \rceil \times h_m \lceil \frac{h}{h_M} \rceil$ , where  $\lceil \cdot \rceil$  is the ceiling function. The effect of this operation is to resize the input image to an integer multiple (by width and height, respectively) of the model width and height. This interpolation step resizes  $\mathbf{X}_t$  into a grid of tiles, with  $T = \lceil \frac{w}{w_M} \rceil \cdot \lceil \frac{h}{h_M} \rceil$  total tiles, each of dimension  $w_m \times h_m$ .

Following this interpolation step, we resize the image tensor of dimension  $C \times w_m \lceil \frac{w}{w_M} \rceil \times h_m \lceil \frac{h}{h_M} \rceil$  (where  $C$  represents the number of color channels) into a 4D tensor consisting of stacked tiles of dimension  $T \times C \times w_m \times h_m$ ; call this tensor  $\mathbf{X}'_t$ . Next, we pass  $\mathbf{X}'_t$  through  $M$ , applying the previously described tensor decomposition procedure, yielding  $\phi(M(\mathbf{X}'_t))$ . We process the tiles through  $M$  as a minibatch of size  $T$  so that this step can be parallelized for improved efficiency of our algorithm.

After generating  $\phi(M(\mathbf{X}'_t))$ , a tensor of dimension  $T \times D_\phi \times w_m \times h_m$ , we finally construct a tessellation of these tile features with respect to their original location in  $\mathbf{X}_t$  (before stacking), giving a

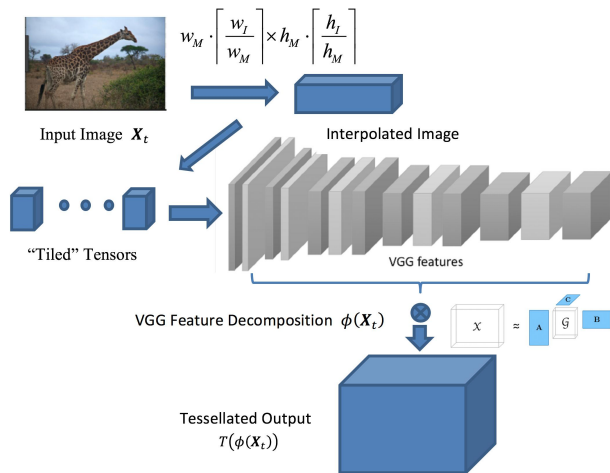


**Figure 5: Schematic of the convolutional tessellation procedure.**

tensor of size  $C \times w_m \lceil \frac{w}{w_M} \rceil \times h_m \lceil \frac{h}{h_M} \rceil$ . We follow this step with a final interpolation to render the tessellation in dimensions equal to the original image. Figure 4 provides a schematic of the deep convolutional tessellation algorithm; Figure 5 compares the fidelity of pre-trained VGG-19 features with and without our tessellation algorithm.

## 2.4 Context-Aware Skip Connections

Recent research [23], [35] has amply demonstrated the value of adding so-called skip connections to deep architectures. Skip connections have been shown to mitigate phenomena such as *vanishing gradient* and per-layer network saturation in deep learning. In general, skip connections are network wirings that allow features from early layers in the network to bypass later layers so that these features remain undiluted. These early features are typically (though not always) concatenated with activations in subsequent layers [23]. The basic intuition behind this approach is that the network is given access to a larger variety of feature representations (e.g. middle layer outputs), as opposed to a strict, hierarchically sequential representation of features.

We introduce a novel variant of these concatenated skip connections in our segmentation network. Instead of traditional skip connections as described in the previous paragraph, we strictly propagate "context features" as skip connections across every layer in our network. By context features, we include the current frame image, the previous frame image, positive and negative user clicks, and positive and negative diffusion user clicks masks. Together, each of these features is concatenated with the previous layer output and then passed to the current layer of the network.

We choose to pass context features in place of previous layer outputs for two basic reasons: (1) context features are high-fidelity, information-rich features with regard to the semantic segmentation task, and they are consequently highly *discriminative*; (2) in addition, by propagating context features as skip connections, we are essentially providing the network with access to features that directly correlate with our model task; in this way the network

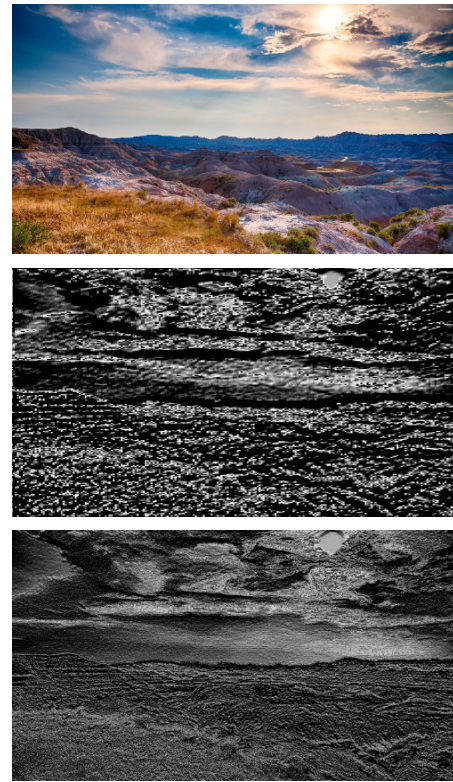


**Figure 6: (Top) Original 2k resolution image; (Middle) non-tessellated deep convolutional feature map generated by VGG-19; (Bottom) tessellated deep convolutional feature map using VGG-19.**

does not need to reserve additional overhead to redundantly encode these task-relevant features in subsequent layers of the network. We show a schematic of context aware skip connections in Figure 2.

## 2.5 VFX Segmentation Dataset

In addition to our segmentation network, we introduce an original, high-resolution dataset intended for pixel-level segmentation tasks in computer vision, the *VFX Segmentation Dataset*. This dataset consists of 27,046 RGB video frames across 208 different video clips, with each frame in 2k resolution ( $1920 \times 1080$ ). Our dataset consists of professionally-filmed human subjects in studio, green screen, and composited scenes; each clip ranges in length from approximately 100-400 frames each. For each video frame, the ground-truth segmentation consists of either a keyed alpha mask (for green screen and composited videos) or a hand-rendered, binary pixel-level segmentation (for non-green screen content). For comparison, the current standard benchmark dataset for high-resolution video segmentation, DAVIS [7], consists of 10,474 frames across 150 video sequences. The *VFX Segmentation Dataset* is particularly suited for training and testing high fidelity segmentation, human subject tracking, and fostering robustness with composited video data (a common usecase with VFX studios). To maintain training parity



**Figure 7: Representative images from the VFX Segmentation Dataset. (Left) Original RGB image; (Right) Hand-generated ground-truth segmentation.**

with other segmentation models, we train our model on only a subset of this dataset in addition to the aforementioned DAVIS dataset (see Section III for details). We show several representative examples of video frames and their corresponding ground-truth segmentations from the *VFX Segmentation Dataset* in Figure 7.

### 3 EXPERIMENTAL RESULTS

Through experiments, we compare the segmentation results generated by our HyperSeg network with several state of the art and baseline models for the interactive image segmentation task. We use two metrics for this evaluation: mean IOU (mIOU) and mean boundary IOU (mBIOU). We define mBIOU as IOU applied between the boundary contours of the ground-truth and generated segmentation masks (after applying a dilation of 1 pixel to each segmentation boundary, respectively). Note, in particular, that mBIOU represents a very high standard for segmentation accuracy, as it reflects a near pixel-level match with the ground-truth segmentation boundary. HyperSeg was trained using 14,326 2k resolution images (8,761 images from the DAVIS dataset and + 5,565 from the VFX Segmentation Dataset) for 85 epochs. During training we generate simulated clicks (per image a random number of between 1-15 positive and negative clicks is rendered) using the click simulation strategy adopted in [48]. For testing, we used a randomly selected set of 1,622 2k resolution images ( $1980 \times 1020$ ) consisting of 849 images from the VFX Segmentation Dataset and 773 images taken from the DAVIS dataset; all the test images were held out from training. For evaluation, we fixed the interactive parameter using 10 total clicks (5 positive and 5 negative). In Figures 8 and 9 we show examples of representative HyperSeg segmentation results on the test data.

In Table I we report experimental results for mIOU and mBIOU for HyperSeg compared with state of the art and baseline models, including ISEG (interactive segmentation) [29], DOS [48], Graph Cut [6] and Random Walk [18]. HyperSeg demonstrates a 19% relative increase in mIOU and 34% relative increase in mBIOU over SOA interactive segmentation models. In Figure 10 we show comparative examples of segmentation results with SOA models; in addition, Figures 11 and 12 highlight the improved smoothness and boundary accuracy exhibited by HyperSeg segmentations; Figure

**Table 1: Segmentation Results**

Method	mIOU	mBIOU
<b>HyperSeg (Ours)</b>	<b>0.840</b>	<b>0.097</b>
ISEG [29]	0.705	0.072
DOS [48]	0.681	0.054
Graph Cut [6]	0.563	0.0
Random Walk [18]	0.639	0.021



**Figure 8: Example HyperSeg segmentation outputs from test data taken from the VFX Segmentation dataset (10 total clicks).**

11 additionally indicates the efficacy of our use of convolutional tensor decomposition for the HyperSeg segmentation output.

### 4 SUMMARY

The current research presents a novel, high density deep learning algorithm for interactive video segmentation tasks that demonstrates a substantial improvement over current state of the art models with respect to both overall segmentation accuracy and segmentation boundary accuracy. Our research provides several key innovations, including: (1) the application of convolutional tensor decomposition to achieve substantial model compression, (2) the introduction of a novel boundary loss function, (3) a convolutional tessellation technique used to render pre-trained features in the native input resolution, (4) the application of "context-aware" skip connections, and (5) the introduction a new benchmark video segmentation dataset, the VFX Segmentation Dataset.

### REFERENCES

- [1] 1996. Region competition: Unifying snakes, region growing, and Bayes/MDL for multiband image segmentation. 18, 9 (SEP 1996), 884–900.
- [2] Michael F. Barnsley and Lyman P. Hurd. 1993. *Fractal Image Compression*. A. K. Peters, Ltd., USA.
- [3] Jonathan T. Barron. 2017. A General and Adaptive Robust Loss Function. (2017). <http://arxiv.org/abs/1701.03077> cite arxiv:1701.03077Comment: CVPR 2019.
- [4] Arnaud Benard and Michael Gygli. 2017. Interactive Video Object Segmentation in the Wild. (12 2017).
- [5] Maxim Berman, Amal Rannen Triki, and Matthew B. Blaschko. 2017. The Lovasz-Softmax Loss: A Tractable Surrogate for the Optimization of the Intersection-Over-Union Measure in Neural Networks. *2018 IEEE/CVF Conference on Computer*



Figure 9: Example HyperSeg segmentation outputs from subset of test data taken from the DAVIS dataset (10 total clicks).

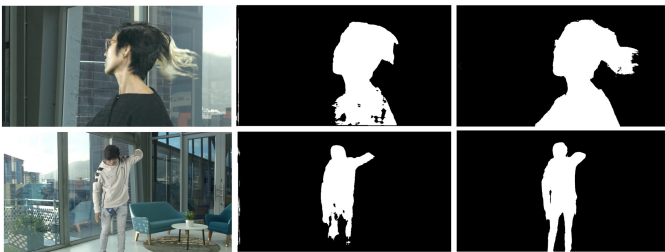


Figure 10: Segmentation quality comparison: (Left) Original 2k input image, (Middle) ISEG [29], (Right) HyperSeg (10 total clicks).

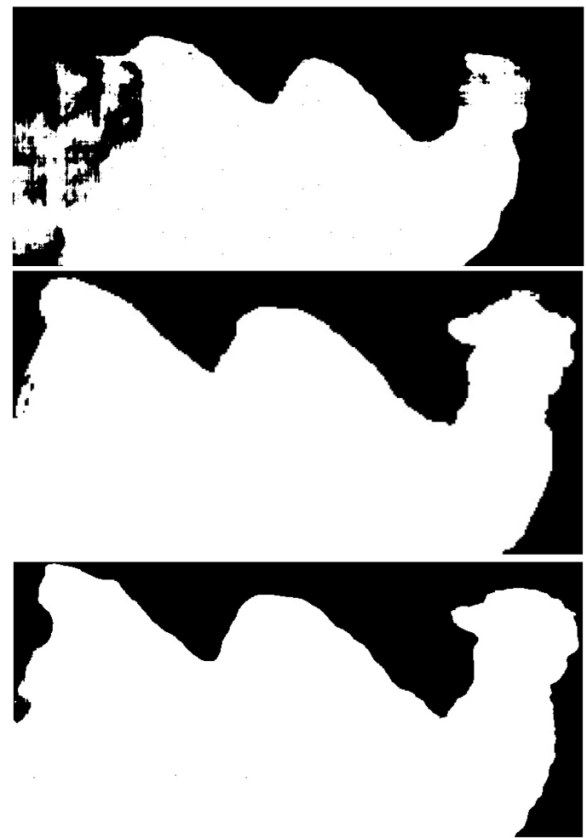


Figure 11: Tensor decomposition and segmentation boundary quality comparison: (Top) result for HyperSeg network trained without Tucker decomposition, using instead a random subset of  $D_\phi = 736$  dense, pre-trained VGG features; (Middle) ISEG [29], (Bottom) HyperSeg with Tucker decomposition; HyperSeg renders smoother, more accurate boundaries in general.



Figure 12: Segmentation boundary quality comparison: (Left) ISEG [29], (Right) HyperSeg.

*Vision and Pattern Recognition* (2017), 4413–4421.

[6] Y.Y. Boykov and M.-P. Jolly. 2001. Interactive graph cuts for optimal boundary; region segmentation of objects in N-D images. In *Computer Vision, 2001. ICCV 2001. Proceedings. Eighth IEEE International Conference on*, Vol. 1. 105–112 vol.1. <https://doi.org/10.1109/ICCV.2001.937505>

[7] Sergi Caelles, Jordi Pont-Tuset, Federico Perazzi, Alberto Montes, Kevis-Kokitsi Maninis, and Luc Van Gool. 2019. The 2019 DAVIS Challenge on VOS: Unsupervised Multi-Object Segmentation. *arXiv:1905.00737* (2019).

[8] Liang-Chieh Chen, George Papandreou, Iasonas Kokkinos, Kevin Murphy, and Alan L. Yuille. 2016. DeepLab: Semantic Image Segmentation with Deep Convolutional Nets, Atrous Convolution, and Fully Connected CRFs. *CoRR* abs/1606.00915 (2016). <http://dblp.uni-trier.de/db/journals/corr/corr1606.html#ChenPK0Y16>

[9] Qifeng Chen and Vladlen Koltun. 2017. Photographic Image Synthesis with Cascaded Refinement Networks. *2017 IEEE International Conference on Computer Vision (ICCV)* (2017), 1520–1529.

[10] Qifeng Chen, Jia Xu, and Vladlen Koltun. 2017. Fast Image Processing with Fully-Convolutional Networks. *2017 IEEE International Conference on Computer Vision (ICCV)* (2017), 2516–2525.

[11] Keh-Shih Chuang, Hong-Long Tzeng, Sharon Chen, Jay Wu, and Tzong-Jer Chen. 2006. Fuzzy c-means clustering with spatial information for image segmentation. *Computerized Medical Imaging and Graphics*, 30, 9–15. *Computerized medical imaging and graphics: the official journal of the Computerized Medical Imaging Society* 30 (02 2006), 9–15. <https://doi.org/10.1016/j.compmedimag.2005.10.001>

[12] G. B. Coleman and H. C. Andrews. 1979. Image segmentation by clustering. *Proc. IEEE* 67, 5 (May 1979), 773–785. <https://doi.org/10.1109/PROC.1979.11327>

[13] N. Dalal and B. Triggs. 2005. Histograms of Oriented Gradients for Human Detection. *Computer Vision and Pattern Recognition, 2005. CVPR 2005. IEEE Computer Society Conference on* 1 (2005), 886–893. <http://ieeexplore.ieee.org/>

- xpls/abs\_all.jsp?arnumber=1467360
- [14] Huawu Deng and David A. Clausi. 2004. Unsupervised Image Segmentation Using a Simple MRF Model with a New Implementation Scheme. *Pattern Recogn.* 37, 12 (Dec. 2004), 2323–2335. <https://doi.org/10.1016/j.patcog.2004.04.015>
  - [15] J. Deng, W. Dong, R. Socher, L.-J. Li, K. Li, and L. Fei-Fei. 2009. ImageNet: A Large-Scale Hierarchical Image Database. In *CVPR09*.
  - [16] Ross Girshick. 2015. Fast R-CNN. In *Proceedings of the 2015 IEEE International Conference on Computer Vision (ICCV) (ICCV '15)*. IEEE Computer Society, USA, 1440–1448. <https://doi.org/10.1109/ICCV.2015.169>
  - [17] Ross Girshick, Jeff Donahue, Trevor Darrell, and Jitendra Malik. 2014. Rich Feature Hierarchies for Accurate Object Detection and Semantic Segmentation. In *Proceedings of the 2014 IEEE Conference on Computer Vision and Pattern Recognition (CVPR '14)*. IEEE Computer Society, USA, 580–587. <https://doi.org/10.1109/CVPR.2014.81>
  - [18] Leo Grady. 2006. Random Walks for Image Segmentation. *IEEE Trans. Pattern Anal. Mach. Intell.* 28, 11 (Nov. 2006), 1768–1783. <https://doi.org/10.1109/TPAMI.2006.233>
  - [19] Lars Grasedyck. 2010. Hierarchical Singular Value Decomposition of Tensors. *SIAM J. Matrix Analysis Applications* 31 (01 2010), 2029–2054. <https://doi.org/10.1137/090764189>
  - [20] O. Haji-Maghsoudi, A. Talebpour, H. Soltanian-Zadeh, and N. Haji-maghsoudi. 2012. 'Automatic organs' detection in WCE. In *The 16th CSI International Symposium on Artificial Intelligence and Signal Processing (AISP 2012)*. 116–121. <https://doi.org/10.1109/AISP.2012.6313729>
  - [21] Bharath Hariharan, Pablo Andrés Arbeláez, Ross B. Girshick, and Jitendra Malik. 2015. Hypercolumns for object segmentation and fine-grained localization.. In *CVPR. IEEE Computer Society*, 447–456. <http://dblp.uni-trier.de/db/conf/cvpr/cvpr2015.html#HariharanAGM15>
  - [22] Kaiming He, Georgia Gkioxari, Piotr Dollár, and Ross B. Girshick. 2017. Mask R-CNN. *2017 IEEE International Conference on Computer Vision (ICCV) (2017)*, 2980–2988.
  - [23] Kaiming He, Xiangyu Zhang, Shaoqing Ren, and Jian Sun. 2015. Deep Residual Learning for Image Recognition. *2016 IEEE Conference on Computer Vision and Pattern Recognition (CVPR) (2015)*, 770–778.
  - [24] Tamara G. Kolda and Brett W. Bader. 2009. Tensor Decompositions and Applications. *SIAM REVIEW* 51, 3 (2009), 455–500.
  - [25] Alex Krizhevsky, Ilya Sutskever, and Geoffrey E. Hinton. 2012. ImageNet Classification with Deep Convolutional Neural Networks. In *Proceedings of the 25th International Conference on Neural Information Processing Systems - Volume 1 (Lake Tahoe, Nevada) (NIPS'12)*. Curran Associates Inc., Red Hook, NY, USA, 1097–1105.
  - [26] Yann Lecun, Léon Bottou, Yoshua Bengio, and Patrick Haffner. 1998. Gradient-based learning applied to document recognition. In *Proceedings of the IEEE*. 2278–2324.
  - [27] Sang Uk Lee, Seok Yoon Chung, and Rae-Hong Park. 1990. A comparative performance study of several global thresholding techniques for segmentation. *Computer Vision, Graphics, and Image Processing* 52, 2 (1990), 171–190. <http://dblp.uni-trier.de/db/journals/cvqip/cvqip52.html#LeeCP90>
  - [28] Yin Li, Jian Sun, Chi-Keung Tang, and Heung-Yeung Shum. 2004. Lazy Snapping. *ACM Trans. Graph.* 23, 3 (Aug. 2004), 303–308. <https://doi.org/10.1145/1015706.1015719>
  - [29] Zhuwen Li, Qifeng Chen, and Vladlen Koltun. 2018. Interactive Image Segmentation with Latent Diversity. *2018 IEEE/CVF Conference on Computer Vision and Pattern Recognition (2018)*, 577–585.
  - [30] Tsung-Yi Lin, Piotr Dollár, Ross Girshick, Kaiming He, Bharath Hariharan, and Serge Belongie. 2016. Feature Pyramid Networks for Object Detection. (12 2016).
  - [31] David G. Lowe. 2004. Distinctive Image Features from Scale-Invariant Keypoints. *International Journal of Computer Vision* 60 (2004), 91–110.
  - [32] Vinod Nair and Geoffrey E. Hinton. 2010. Rectified Linear Units Improve Restricted Boltzmann Machines. In *Proceedings of the 27th International Conference on Machine Learning (ICML-10)*, Johannes Fürnkranz and Thorsten Joachims (Eds.), 807–814.
  - [33] Hieu Tat Nguyen, Marcel Worring, and Rein Van Den Boomgaard. 2003. Watersnakes: energydriven watershed segmentation. *IEEE Transactions on Pattern Analysis and Machine Intelligence* (2003), 330–342.
  - [34] Kang-Yu Ni, Xavier Bresson, Tony Chan, and Selim Esedoglu. 2009. Local Histogram Based Segmentation Using the Wasserstein Distance. *International Journal of Computer Vision* 84 (08 2009), 97–111. <https://doi.org/10.1007/s11263-009-0234-0>
  - [35] Taesung Park, Ming-Yu Liu, Ting-Chun Wang, and Jun-Yan Zhu. 2019. Semantic Image Synthesis with Spatially-Adaptive Normalization. In *Proceedings of the IEEE Conference on Computer Vision and Pattern Recognition*.
  - [36] Stephan Rabanser, Aleksandr Shchur, and Stephan Günnemann. 2017. Introduction to Tensor Decompositions and their Applications in Machine Learning. <http://arxiv.org/abs/1711.10781> cite arxiv:1711.10781Comment: 13 pages, 12 figures.
  - [37] Joseph Redmon, Santosh Divvala, Ross Girshick, and Ali Farhadi. 2015. You Only Look Once: Unified, Real-Time Object Detection. <http://arxiv.org/abs/1506.02640>.
  - [38] Shaoqing Ren, Kaiming He, Ross Girshick, and Jian Sun. 2015. Faster R-CNN: Towards Real-Time Object Detection with Region Proposal Networks. In *Proceedings of the 28th International Conference on Neural Information Processing Systems - Volume 1 (Montreal, Canada) (NIPS'15)*. MIT Press, Cambridge, MA, USA, 91–99.
  - [39] O. Ronneberger, P.Fischer, and T. Brox. 2015. U-Net: Convolutional Networks for Biomedical Image Segmentation. In *Medical Image Computing and Computer-Assisted Intervention (MICCAI) (LNCS, Vol. 9351)*. Springer, 234–241. <http://lmb.informatik.uni-freiburg.de/Publications/2015/RFB15a> (available on arXiv:1505.04597 [cs.CV]).
  - [40] Evan Shelhamer, Jonathon Long, and Trevor Darrell. 2016. Fully Convolutional Networks for Semantic Segmentation. *IEEE Transactions on Pattern Analysis and Machine Intelligence* 39 (05 2016), 1–1. <https://doi.org/10.1109/TPAMI.2016.2572683>
  - [41] Karen Simonyan and Andrew Zisserman. 2015. Very Deep Convolutional Networks for Large-Scale Image Recognition. In *International Conference on Learning Representations*.
  - [42] Christian Szegedy, Wei Liu, Yangqing Jia, Pierre Sermanet, Scott Reed, Dragomir Anguelov, Dumitru Erhan, Vincent Vanhoucke, and Andrew Rabinovich. 2015. Going Deeper with Convolutions. In *Computer Vision and Pattern Recognition (CVPR)*. <http://arxiv.org/abs/1409.4842>
  - [43] Jen Hong Tan and U Rajendra Acharya. 2014. Active spline model: A shape based model - Interactive segmentation. *Digital Signal Processing* 35 (09 2014), <https://doi.org/10.1016/j.dsp.2014.09.002>
  - [44] O. J. Tobias and R. Seara. 2002. Image segmentation by histogram thresholding using fuzzy sets. *IEEE Transactions on Image Processing* 11, 12 (Dec 2002), 1457–1465. <https://doi.org/10.1109/TIP.2002.806231>
  - [45] Guotai Wang, Wenqi Li, Maria A. Zuluaga, Rosalind Pratt, Premal A. Patel, Michael Aertsen, Tom Doel, Anna L. David, Jan Deprest, Sebastien Ourselin, and Tom Vercauteren. 2018. Interactive Medical Image Segmentation using Deep Learning with Image-specific Fine-tuning. *IEEE Transactions on Medical Imaging* (26 1 2018). <https://doi.org/10.1109/TMI.2018.2791721>
  - [46] G. Wang, W. Li, M. A. Zuluaga, R. Pratt, P. A. Patel, M. Aertsen, T. Doel, A. L. David, J. Deprest, S. Ourselin, and T. Vercauteren. 2018. Interactive Medical Image Segmentation Using Deep Learning With Image-Specific Fine Tuning. *IEEE Transactions on Medical Imaging* 37, 7 (July 2018), 1562–1573. <https://doi.org/10.1109/TMI.2018.2791721>
  - [47] Tinghuai Wang, Bo Han, and John Collomosse. 2014. TouchCut: Fast Image and Video Segmentation Using Single-Touch Interaction. *Comput. Vis. Image Underst.* 120 (March 2014), 14–30. <https://doi.org/10.1016/j.cviu.2013.10.013>
  - [48] Ning Xu, Brian L. Price, Scott Cohen, Jimel Yang, and Thomas S. Huang. 2016. Deep Interactive Object Selection. *2016 IEEE Conference on Computer Vision and Pattern Recognition (CVPR) (2016)*, 373–381.
  - [49] xxx. 2018. Light-Weight RefineNet for Real-Time Semantic Segmentation. arXiv:1810.03272 <http://arxiv.org/abs/1810.03272>
  - [50] Allen Y. Yang, John Wright, Yi Ma, and S. Shankar Sastry. 2008. Unsupervised Segmentation of Natural Images via Lossy Data Compression. *Comput. Vis. Image Underst.* 110, 2 (May 2008), 212–225. <https://doi.org/10.1016/j.cviu.2007.07.005>
  - [51] Fisher Yu and Vladlen Koltun. 2016. Multi-Scale Context Aggregation by Dilated Convolutions. In *International Conference on Learning Representations (ICLR)*.
  - [52] Zhong-Qiu Zhao, Peng Zheng, Shou-tao Xu, and Xindong Wu. 2018. Object Detection with Deep Learning: A Review. <http://arxiv.org/abs/1807.05511> cite arxiv:1807.05511.
  - [53] Shuai Zheng, Sadeep Jayasumana, Bernardino Romera-Paredes, Vibhav Vineet, Zhizhong Su, Dalong Du, Chang Huang, and Philip H. S. Torr. 2015. Conditional Random Fields as Recurrent Neural Networks. In *Proceedings of the 2015 IEEE International Conference on Computer Vision (ICCV) (ICCV '15)*. IEEE Computer Society, USA, 1529–1537. <https://doi.org/10.1109/ICCV.2015.179>
  - [54] Yi Zhou, Xiaodong He, Lei Huang, Li Liu, Fan Zhu, Shanshan Cui, and Ling Shao. 2019. Collaborative Learning of Semi-Supervised Segmentation and Classification for Medical Images. In *The IEEE Conference on Computer Vision and Pattern Recognition (CVPR)*.